

DESC: A Stellarator Equilibrium Solver

D. W. Dudt^{1, a)} and E. Kolemen^{1, b)}

Princeton University, Princeton, New Jersey 08544

(Dated: 24 September 2020)

The new code DESC is presented to solve for fixed-boundary ideal MHD equilibria in stellarators. The approach directly solves the equilibrium force balance as a system of nonlinear equations in the form $\mathbf{f}(\mathbf{x}) = \mathbf{0}$. The independent variables \mathbf{x} represent nested magnetic flux surfaces expressed in the inverse representation with toroidal flux coordinates, and the equations $\mathbf{f}(\mathbf{x})$ quantify equilibrium force balance errors at discrete points in real space. Discretizing with global Fourier-Zernike basis functions properly treats the magnetic axis and minimizes the number of coefficients needed to describe the flux surfaces. The pseudospectral method provides great flexibility in where the errors are evaluated, and the system of equations is efficiently solved with a Newton-Raphson iteration. Equilibria are computed and compared against VMEC for both axisymmetric and non-axisymmetric examples. The results show fast convergence rates and solutions with low errors throughout the plasma volume.

I. INTRODUCTION

A. Equilibrium Problem

Magnetic confinement in toroidal devices such as the tokamak and stellarator presents the most promising approach to controlled nuclear fusion. Optimizing the design and performance of these reactors to continue improving their performance relies on fast and accurate numerical calculations of the equilibrium plasma state. Under the ideal magnetohydrodynamic (MHD) model, the equilibrium for a static plasma is given by the force balance equation, and Ampère's and Gauss's laws:

$$\mathbf{J} \times \mathbf{B} = \nabla p \quad (1a)$$

$$\nabla \times \mathbf{B} = \mu_0 \mathbf{J} \quad (1b)$$

$$\nabla \cdot \mathbf{B} = 0. \quad (1c)$$

An equilibrium is a magnetic field \mathbf{B} that solves this system of nonlinear partial differential equations (PDEs), subject to the pressure profile p and any additional constraints.

In the axisymmetric case of tokamaks, the resulting Grad-Shafranov equation is numerically tractable, and codes have been developed to efficiently solve this elliptic PDE¹. Stellarators are inherently three-dimensional² (3-D), however, and the simplification of an ignorable coordinate cannot be used. Promising experimental results in recent years have led to a renewed interest in stellarators³, and the search for an optimal design is leading to high-beta configurations with complicated geometries. Although there are existing codes for handling 3-D equilibria, they are inadequate for machine learning and real-time applications and for studying the full phase-space of stellarator configurations.

B. Literature Review

The first equilibrium codes developed specifically for 3-D toroidal geometries were based on the MHD variational

principle⁴, and used finite difference approximations in the discretization of all three spatial coordinates. Chodura and Schlüter⁵ proposed to directly solve the equilibrium problem by minimizing the total potential energy of the plasma on a space-fixed Eulerian grid. The BETA⁶ code instead solves the “inverse” equilibrium problem, which finds the toroidal flux coordinates instead of directly solving for the magnetic field. The major drawbacks of these approaches are that they assume the existence of nested flux surfaces and their accuracy is limited to second-order by the finite difference schemes.

It was quickly realized that these algorithms could be greatly improved with spectral methods⁷. Bhattacharjee, Wiley and Dewar⁸ proposed a variational method with the inverse mapping using Fourier series representations of the poloidal and toroidal angles. The NEAR⁹ code replaced the discretization of Chodura and Schlüter with a similar scheme, and also changed the Eulerian grid to employ a vacuum flux coordinate system. Similarly, VMEC¹⁰ was developed as the spectral version of the inverse energy principle used by BETA. This increased the speed and accuracy of calculations, and VMEC has become the most widely-adopted stellarator equilibrium code. However, both of these approaches still use simple finite differences in their radial discretizations, and are only first-order accurate at the magnetic axis. Additionally, the assumption of nested flux surfaces is known to cause issues at rational surfaces¹¹.

Several codes have since been developed to allow for magnetic islands and regions of stochastic field-lines, since nested flux surfaces generally do not exist in 3D equilibria. The BETA code was modified into BETAS¹² to allow for magnetic islands, and it also updated to Fourier decompositions for the angular coordinates. A nonvariational approach is taken by HINT¹³, which introduces artificial resistivity and viscosity and integrates in time until the plasma has relaxed to an equilibrium. This code uses a fixed-space Eulerian grid with second-order accurate finite differences, much like the approach of Chodura and Schlüter. But unlike most other codes which conserve the total magnetic flux inside the torus, HINT instead solves for currentless stellarator equilibria.

Recognizing that relaxation methods need to resolve small time scales that slow down convergence, the PIES¹⁴ code employs a different algorithm: it iteratively calculates the pres-

^{a)}ddudt@princeton.edu

^{b)}ekolemen@princeton.edu

sure driven current from a magnetic field and then updates that field using Ampère's law. Similar to NEAR and VMEC, PIES utilizes a combination of Fourier modes and centered finite differences to discretize the volume. SIESTA¹⁵ is another iterative solver based on the energy principle, which starts from a perturbed VMEC solution and can handle more complicated field-line behavior than BETAS. This code uses pseudospectral techniques and a staggered radial grid to better treat the magnetic axis, but the radial mesh is still only second-order accurate.

SPEC¹⁶ allows for complicated field behavior by dividing the domain into regions of constant pressure that are separated by a discrete number of irrational surfaces, and finite element methods are used to represent the subdomains with Fourier and Chebyshev basis functions. The algorithm does not solve the MHD force balance with a finite pressure gradient, it requires discontinuous inputs that may not represent realistic profiles, and it does not properly resolve the magnetic axis.

C. Benefits of a New Method

Despite the progress in this field, there is still demand for an equilibrium code that is fast, accurate, and flexible for many secondary applications. This paper presents a new code, called DESC, that aims to fulfill this need by directly solving the equilibrium equations in the most efficient manner while also providing a useful format for stellarator optimization. The approach is currently formulated for fixed-boundary problems, but will be extended to free-boundary equilibria. Like VMEC, nested flux surfaces are assumed to exist. Although this assumption is rarely true for real plasmas, it provides crucial simplifications and ensures that any solution will be of practical interest for good confinement. Rather than minimizing the total energy of the plasma, the MHD equilibrium equations are solved in the form of a nonlinear system $\mathbf{f}(\mathbf{x}) = \mathbf{0}$, where the output $\mathbf{f}(\mathbf{x})$ corresponds to the force balance error at discrete points in physical space and must vanish in equilibrium. The potential advantages of this approach are numerous:

1. Solving the force balance equations directly in real space, instead of indirectly through the energy principle, guarantees low residual force errors throughout the plasma volume.
2. Pseudospectral methods minimize the dimensionality of the system, so similar levels of accuracy can be achieved with fewer variables compared to finite difference and finite element techniques.
3. Global basis functions give the solution everywhere in the domain, unlike finite difference methods that are only defined at discrete surfaces.
4. Fourier-Zernike basis functions are used to inherently satisfy the necessary conditions at the coordinate singularity, so the magnetic axis is properly resolved.

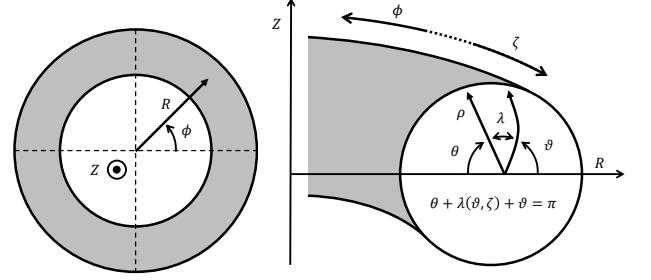


FIG. 1. Toroidal (R, ϕ, Z) and straight field-line (ρ, ϑ, ζ) coordinate systems.

5. Collocation points can be chosen to avoid rational surfaces, where the assumption of nested flux surfaces is not valid.
6. The system of equations can be solved with a Newton-Raphson method, which converges quadratically in the neighborhood of the solution.
7. Unlike the energy principle, it is trivial to find neighboring solutions and vary quantities of interest to locate solution branches once an equilibrium is calculated.

These numerical methods allow this approach to maximize computational speed and accuracy, and they yield significant performance improvements over existing codes.

II. DERIVATION OF PROBLEM FORMULATION

A. Magnetic Field in Toroidal Flux Coordinates

The toroidal flux coordinate system (ρ, ϑ, ζ) is depicted in Figure 1. This is very similar to the coordinate system used by the stability code PEST¹⁷, except that the toroidal angle is chosen as $\zeta = -\phi$ so that the coordinate system is right-handed when the straight field-line poloidal angle ϑ is measured counter-clockwise from the outboard midplane. The covariant basis vectors are defined by $\mathbf{e}_\alpha = [\partial_\alpha R, \partial_\alpha \phi, \partial_\alpha Z]^T$, and the Jacobian of the coordinate system is $\sqrt{g} = \mathbf{e}_\rho \cdot \mathbf{e}_\vartheta \times \mathbf{e}_\zeta$. The flux surface label is chosen to be $\rho = \sqrt{\psi/\psi_a}$ where ψ_a is the toroidal magnetic flux at the last closed flux surface, so that ρ is proportional to the minor radius. Note that this choice differs from the default radial coordinate in VMEC of ψ/ψ_a , which results in a lower density of flux surfaces near the magnetic axis and can affect its resolution accordingly.

Any vector, including the magnetic field, can be written in contravariant form as

$$\mathbf{B} = B^\rho \mathbf{e}_\rho + B^\vartheta \mathbf{e}_\vartheta + B^\zeta \mathbf{e}_\zeta. \quad (2)$$

Under the assumption that nested flux surfaces exist $\mathbf{B} \cdot \nabla \rho = B^\rho = 0$, so the representation reduces to $\mathbf{B} = B^\vartheta \mathbf{e}_\vartheta + B^\zeta \mathbf{e}_\zeta$. B^ϑ and B^ζ are not independent but are related through (1c) by

$$B^\vartheta = -\frac{1}{\sqrt{g}} \frac{\partial \alpha}{\partial \zeta} \quad (3a)$$

$$B^\zeta = \frac{1}{\sqrt{g}} \frac{\partial \alpha}{\partial \vartheta} \quad (3b)$$

where $\alpha(\rho, \vartheta, \zeta)$ is some stream function. This leads to the Clebsch representation

$$\mathbf{B} = \nabla \rho \times \nabla \alpha(\rho, \vartheta, \zeta) \quad (4)$$

which reveals that magnetic field-lines lie on surfaces of constant ρ (flux surfaces) and surfaces of constant α . Equations (2)-(4) could describe magnetic surfaces in any toroidal coordinate system with arbitrary angle definitions, but ϑ and ζ are chosen to be straight field-line coordinates. Since the toroidal angle is fixed as $\zeta = -\phi$, this necessitates a particular definition for ϑ . The function

$$\theta(\vartheta, \zeta) = \pi - \vartheta - \lambda(\vartheta, \zeta) \quad (5)$$

is used to relate the straight field-line angle ϑ to a more general poloidal angle θ , such as one that demarks constant arc lengths. λ is a periodic function of both ϑ and ζ with zero average over a flux surface, and the factor of π is necessary to convert between the clockwise and counter-clockwise directions.

The “straightness” of the (ρ, ϑ, ζ) coordinate system is satisfied with the following choice for the stream function¹⁸:

$$\alpha(\rho, \vartheta, \zeta) = \frac{1}{2\pi} (\psi' \vartheta - \chi' \zeta). \quad (6)$$

Here $\psi(\rho)$ and $\chi(\rho)$ are the toroidal and poloidal magnetic flux, respectively, and the prime denotes a derivative with respect to ρ . Therefore the equation for a magnetic field-line on the flux surface $\rho = \rho_0$ is $\vartheta - \iota \zeta = \text{constant}$, which is the desired equation of a straight line with a slope equal to the rotational transform:

$$\iota(\rho) = \frac{d\vartheta}{d\zeta} = \frac{B^\vartheta}{B^\zeta} = \frac{\chi'}{\psi'}. \quad (7)$$

Combining (2)-(7) yields an expression for the magnetic field with nested flux surfaces in contravariant form of the straight field-line coordinate system:

$$\mathbf{B} = B^\vartheta \mathbf{e}_\vartheta + B^\zeta \mathbf{e}_\zeta = \frac{\psi'}{2\pi\sqrt{g}} (\iota \mathbf{e}_\vartheta + \mathbf{e}_\zeta) \quad (8)$$

This formulation reveals the well known principle that magnetic field-lines constitute a one-and-a-half-degree-of-freedom Hamiltonian system¹⁹. The canonical position, momentum, and time become ϑ , ψ , and ζ , respectively, in the magnetic coordinate system (ψ, ϑ, ζ) . When toroidal flux surfaces exist, the Hamiltonian $\chi(\psi)$ is a flux surface quantity, and Hamilton’s equations become:

$$\frac{d\vartheta}{d\zeta} = \frac{\partial \chi}{\partial \psi} = \iota \quad (9a)$$

$$\frac{d\psi}{d\zeta} = -\frac{\partial \chi}{\partial \vartheta} = 0. \quad (9b)$$

B. Force Balance Equations

Combining (1a) and (1b), a force balance error \mathbf{F} can be defined as

$$\mathbf{F} \equiv \frac{1}{\mu_0} (\nabla \times \mathbf{B}) \times \mathbf{B} - \nabla p = \mathbf{0}, \quad (10)$$

and the equilibrium magnetic field must satisfy this equation. Substituting the form of the field from (8) into the force balance error (10) yields¹⁰

$$\mathbf{F} = F_\rho \nabla \rho + F_\beta \beta \quad (11a)$$

$$F_\rho = \sqrt{g} (B^\zeta J^\vartheta - B^\vartheta J^\zeta) - p' \quad (11b)$$

$$= \frac{1}{\mu_0} (B^\zeta (\partial_\zeta B_\rho - \partial_\rho B_\zeta) - B^\vartheta (\partial_\rho B_\vartheta - \partial_\vartheta B_\rho)) - p'$$

$$F_\beta = \sqrt{g} J^p = \frac{1}{\mu_0} (\partial_\vartheta B_\zeta - \partial_\zeta B_\vartheta) \quad (11c)$$

$$\beta = B^\zeta \nabla \vartheta - B^\vartheta \nabla \zeta. \quad (11d)$$

This reveals that there are only two independent components of the force balance error \mathbf{F} : a radial component F_ρ and a helical component denoted F_β . These vector components can be written as a system of two scalar equations that represent the total force error (in Newtons) in a volume of plasma:

$$f_\rho = F_\rho \|\nabla \rho\|_2 \sqrt{g} \Delta \rho \Delta \vartheta \Delta \zeta \text{sign}(\nabla \rho \cdot \mathbf{e}_\rho) \quad (12a)$$

$$f_\beta = F_\beta \|\beta\|_2 \sqrt{g} \Delta \rho \Delta \vartheta \Delta \zeta \text{sign}(\beta \cdot \mathbf{e}_\vartheta) \text{sign}(\beta \cdot \mathbf{e}_\zeta). \quad (12b)$$

See Appendix A for a complete derivation of these equations and their special treatment at the magnetic axis. Equations (10)-(12) are expressed in terms of the magnetic field, but the only independent variables are R and Z as they appear in the covariant basis vectors. Therefore, given the shapes of the flux surfaces in the plasma volume, $R(\rho, \vartheta, \zeta)$ and $Z(\rho, \vartheta, \zeta)$, the force balance errors $f_\rho(\rho, \vartheta, \zeta)$ and $f_\beta(\rho, \vartheta, \zeta)$ can be computed throughout the domain. Both of these equations must vanish in equilibrium.

III. NUMERICAL METHODS

Pseudospectral methods are employed to solve the equilibrium force balance PDE given by (12). This approach is chosen over finite element or finite difference methods because global basis functions converge exponentially. In other words, spectral methods can achieve lower errors for the same dimensionality or reach comparable accuracy with fewer degrees of freedom, at least for regular domains²⁰. The term “pseudospectral” is used to indicate that the equations are forced to vanish at a set of collocation points. The loss in accuracy compared to Galerkin methods is typically negligible at high resolutions, and pseudospectral methods are much simpler to implement²⁰.

A. Spatial Discretization

A Fourier-Zernike^{21–25} basis set is used with “fringe” indexing^{26,27} of the form:

$$R(\rho, \vartheta, \zeta) = \sum_{n=-N}^N \sum_{m=-M}^M \sum_{l \in L} R_{lmn} \mathcal{Z}_l^m(\rho, \vartheta) \mathcal{F}^n(\zeta) \quad (13a)$$

$$Z(\rho, \vartheta, \zeta) = \sum_{n=-N}^N \sum_{m=-M}^M \sum_{l \in L} Z_{lmn} \mathcal{Z}_l^m(\rho, \vartheta) \mathcal{F}^n(\zeta) \quad (13b)$$

where $L = |m|, |m| + 2, |m| + 4, \dots, 2M - |m|$. The standard indexing scheme was also tested, but the fringe indices were determined to be more efficient. $\mathcal{F}^n(\zeta)$ is the toroidal Fourier series defined as

$$\mathcal{F}^n(\zeta) = \begin{cases} \cos(|n|N_{FP}\zeta) & \text{for } n \geq 0 \\ \sin(|n|N_{FP}\zeta) & \text{for } n < 0 \end{cases} \quad (14)$$

where N_{FP} is the number of field periods of the device (discrete toroidal symmetry). $\mathcal{Z}_l^m(\rho, \vartheta)$ are the Zernike polynomials defined on the unit disc $0 \leq \rho \leq 1, \vartheta \in [0, 2\pi)$ as

$$\mathcal{Z}_l^m(\rho, \vartheta) = \begin{cases} \mathcal{R}_l^{|m|}(\rho) \cos(|m|\vartheta) & \text{for } m \geq 0 \\ \mathcal{R}_l^{|m|}(\rho) \sin(|m|\vartheta) & \text{for } m < 0 \end{cases} \quad (15)$$

with the radial function

$$\mathcal{R}_l^{|m|}(\rho) = \sum_{s=0}^{(l-|m|)/2} \frac{(-1)^s (l-s)!}{s! [\frac{1}{2}(l+|m|)-s]! [\frac{1}{2}(l-|m|)-s]!} \rho^{l-2s}. \quad (16)$$

Zernike polynomials are orthogonal on the unit disc with the inner product

$$\langle A, B \rangle = \int_0^{2\pi} \int_0^1 A(\rho, \vartheta) B(\rho, \vartheta) \rho d\rho d\vartheta, \quad (17)$$

and the normalization is chosen such that

$$\langle \mathcal{Z}_l^m, \mathcal{Z}_{l'}^{m'} \rangle = \frac{2(l+1)\delta_{ll'}\delta_{mm'}}{\pi(1+\delta_{m0})} \quad (18)$$

where δ_{ij} is the Kronecker delta. The Zernike polynomials for $M = 2$ are depicted in Figure 2.

For computation, the Fourier-Zernike series is truncated at a poloidal resolution M and a toroidal resolution N . The maximum radial resolution is then ρ^{2M} as dictated by the Zernike polynomials. An advantage of the Zernike polynomials is that the number of basis functions scales as $M^2/2$, meaning it can achieve the same accuracy with about half of the terms that would be necessary in other methods that scale as M^2 , such as the popular Chebyshev-Fourier basis²⁸. A benefit of the global spectral discretization is that (13a-13b) can be interpolated anywhere in the domain $\rho \in [0, 1], \vartheta \in [0, 2\pi), \zeta \in [0, 2\pi)$. Additionally, all partial derivatives of R and Z are known analytically by differentiating the basis functions. Interpolation and/or differentiation therefore reduces to simple matrix multiplication of the spectral coefficients, and the appropriate Vandermonde matrices can be pre-computed. Horner's method²⁹ is used to evaluate the polynomials rather than the Zernike recurrence relations, since this was found to be more numerically stable at low values of ρ .

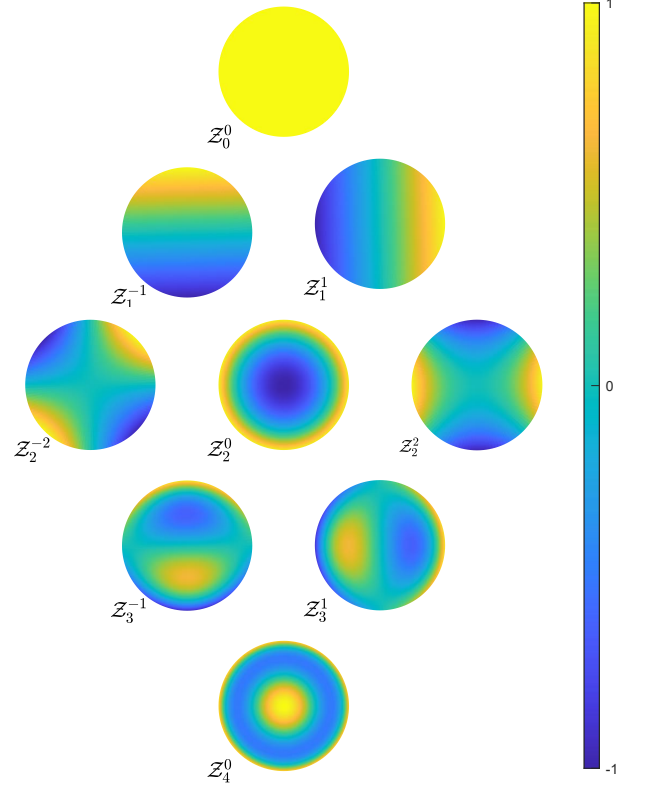


FIG. 2. First nine Zernike polynomials in the fringe ordering, depicting the basis functions used for resolution $M = 2$.

B. Boundary Condition: Magnetic Axis

When an analytic function is expanded near the origin of a disc, the resulting polynomial-Fourier expansion must obey a certain structure²⁸. Suppose the function $f(\rho, \vartheta)$ in polar coordinates is expanded in a real Fourier series as

$$f(x, y) = \sum_{m=0}^{\infty} a_m(\rho) \cos(m\vartheta) + \sum_{m=0}^{\infty} b_m(\rho) \sin(m\vartheta) \quad (19)$$

where $x = \rho \cos \vartheta$ and $y = \rho \sin \vartheta$. It was proved by Lewis and Bellan³⁰ that the radial parity of the Fourier coefficients and their nonsingularity at the origin implies the following form for the radial functions:

$$a_m(\rho) = \rho^m (a_{m,0} + a_{m,2}\rho^2 + a_{m,4}\rho^4 + \dots) \quad (20a)$$

$$b_m(\rho) = \rho^m (b_{m,0} + b_{m,2}\rho^2 + b_{m,4}\rho^4 + \dots). \quad (20b)$$

The variables R and Z are physical quantities representing the locations of flux surfaces, and therefore the scalar functions $R(\rho, \vartheta, \zeta)$ and $Z(\rho, \vartheta, \zeta)$ must be analytic everywhere in the toroidal domain. The Fourier-Zernike basis described by (13a-13b) inherently satisfies the conditions of (19-20), so no special treatment is needed to represent the location of the magnetic axis at $\rho = 0$. This is an advantage over other discretizations that must impose boundary conditions to meet these criteria.

C. Boundary Condition: Last Closed Flux Surface

For a fixed-boundary equilibrium, the surface of the plasma boundary is input as a double Fourier series of the form:

$$R^b(\theta, \phi) = \sum_{n=-N}^N \sum_{m=-M}^M R_{mn}^b \mathcal{G}_n^m(\theta, \phi) \quad (21a)$$

$$Z^b(\theta, \phi) = \sum_{n=-N}^N \sum_{m=-M}^M Z_{mn}^b \mathcal{G}_n^m(\theta, \phi) \quad (21b)$$

$$\mathcal{G}_n^m(\theta, \phi) = \begin{cases} \cos(|m|\theta) \cos(|n|N_{FP}\phi) & \text{for } m \geq 0, n \geq 0 \\ \cos(|m|\theta) \sin(|n|N_{FP}\phi) & \text{for } m \geq 0, n < 0 \\ \sin(|m|\theta) \cos(|n|N_{FP}\phi) & \text{for } m < 0, n \geq 0 \\ \sin(|m|\theta) \sin(|n|N_{FP}\phi) & \text{for } m < 0, n < 0. \end{cases} \quad (21c)$$

The parameterization in (21a-21b) determines the poloidal angle θ . The boundary inputs used in Section IV give an angle measured clockwise from the inboard midplane as shown in Figure 1, but this does not have to be the case in general. This angle θ used to define the boundary surface is related to the straight field-line angle ϑ through $\lambda(\vartheta, \zeta)$ as defined in (5). The stream function λ is given by the double Fourier series

$$\lambda(\vartheta, \zeta) = \sum_{n=-N}^N \sum_{m=-M}^M \lambda_{mn} \mathcal{G}_n^m(\vartheta, \zeta) \quad (22a)$$

$$\mathcal{G}_n^m(\vartheta, \zeta) = \begin{cases} \cos(|m|\vartheta) \cos(|n|N_{FP}\zeta) & \text{for } m \geq 0, n \geq 0 \\ \cos(|m|\vartheta) \sin(|n|N_{FP}\zeta) & \text{for } m \geq 0, n < 0 \\ \sin(|m|\vartheta) \cos(|n|N_{FP}\zeta) & \text{for } m < 0, n \geq 0 \\ \sin(|m|\vartheta) \sin(|n|N_{FP}\zeta) & \text{for } m < 0, n < 0 \end{cases} \quad (22b)$$

along with the constraint

$$\sum_{n=0}^N \sum_{m=0}^M \lambda_{mn} = 0 \quad (23)$$

which ensures that $\lambda(0, 0) = 0$ in order to fix the gauge freedom of the coordinate angles. λ is used in a similar way by VMEC to convert arbitrary poloidal coordinates to the straight field-line angle, but in this context λ is only defined at the plasma boundary ($\rho = 1$).

Using λ to convert from θ to ϑ and recalling that $\phi = -\zeta$ by definition, the boundary can be rewritten as a Fourier series in the straight-field line coordinates:

$$R^b(\vartheta, \zeta) = \sum_{n=-N}^N \sum_{m=-M}^M \tilde{R}_{mn}^b \mathcal{G}_n^m(\vartheta, \zeta) \quad (24a)$$

$$Z^b(\vartheta, \zeta) = \sum_{n=-N}^N \sum_{m=-M}^M \tilde{Z}_{mn}^b \mathcal{G}_n^m(\vartheta, \zeta). \quad (24b)$$

The nonlinear transformation from R_{mn}^b and Z_{mn}^b to \tilde{R}_{mn}^b and \tilde{Z}_{mn}^b is performed in the standard pseudospectral practice of interpolation to real space followed by a Fourier transform, with the “three-halves rule” used to prevent spectral aliasing³¹. The

coefficients from (24a-24b) are then used to provide boundary conditions on the coefficients in (13a-13b). Noting that the radial component of the Zernike basis $\mathcal{R}_l^{|m|}(\rho = 1) = 1$ for all l, m , the explicit boundary conditions are

$$\sum_{l \in L} R_{lmn} = \tilde{R}_{mn}^b \quad (25a)$$

$$\sum_{l \in L} Z_{lmn} = \tilde{Z}_{mn}^b. \quad (25b)$$

This ensures that $R(\rho = 1, \vartheta, \zeta)$ and $Z(\rho = 1, \vartheta, \zeta)$ will match the surface given by $R^b(\theta, \phi)$ and $Z^b(\theta, \phi)$, up to the provided spectral accuracy.

The full Fourier-Zernike basis set defined in (13a-13b) requires $(M+1)^2(2N+1)$ total coefficients, but (25a-25b) provides constraint equations to determine $(2M+1)(2N+1)$ of those coefficients. Similarly, there are a total of $(2M+1)(2N+1)$ coefficients in the double Fourier basis of (22), but one is dependent on the others through (23). Instead of using a spectral tau method where these boundary conditions provide additional equations to be solved²⁰, the constraints are explicitly enforced. For example, R is only given by coefficients up to order $M-1$ in (13a) and the other coefficients are set to ensure that (25a) is satisfied to order M . This approach is chosen over the tau method because it reduces the total number of independent variables and eliminates the need to normalize boundary equations relative to the force balance equations. Combining the spectral representations for R , Z , and λ , it requires a total of $(2M^2 + 2M + 1)(2N + 1) - 1$ variables to completely describe an equilibrium configuration. This scaling of $4M^2N$ variables is a factor of 3 lower than the $\sim 12M^2N$ variables used by the VMEC discretization, assuming M flux surfaces are used in the VMEC calculation (typically it is much higher). These savings can be attributed to the proper treatment of the boundary conditions at the magnetic axis. There are implicit constraint equations caused by the coordinate singularity that VMEC must account for but are inherently satisfied by the Zernike basis functions, as explained in the previous section.

D. Stellarator Symmetry

All current and planned stellarator experiments exhibit stellarator symmetry, and this option can be used to simplify the Fourier-Zernike basis set. Stellarator symmetry is defined as³²

$$R(\rho, -\vartheta, -\zeta) = R(\rho, \vartheta, \zeta) \quad (26a)$$

$$Z(\rho, -\vartheta, -\zeta) = -Z(\rho, \vartheta, \zeta) \quad (26b)$$

and implies “up-down” symmetry in the $\zeta = 0$ plane³³. The symmetric variables can be written in a double Fourier series

of the form

$$R(\rho, \vartheta, \zeta) = \sum_{m,n} R_{mn}(\rho) \cos(m\vartheta - nN_{FP}\zeta) \quad (27a)$$

$$Z(\rho, \vartheta, \zeta) = \sum_{m,n} Z_{mn}(\rho) \sin(m\vartheta - nN_{FP}\zeta) \quad (27b)$$

$$\lambda(\vartheta, \zeta) = \sum_{m,n} \lambda_{mn} \sin(m\vartheta - nN_{FP}\zeta). \quad (27c)$$

Using Ptolemy's identities and truncating to a finite series, this is equivalent to

$$R(\rho, \vartheta, \zeta) = \sum_{n=-N}^{-1} \sum_{m=-M}^{-1} R_{mn}(\rho) \mathcal{G}_n^m(\vartheta, \zeta) \quad (28a)$$

$$+ \sum_{n=0}^N \sum_{m=0}^M R_{mn}(\rho) \mathcal{G}_n^m(\vartheta, \zeta)$$

$$Z(\rho, \vartheta, \zeta) = \sum_{n=-N}^{-1} \sum_{m=0}^M Z_{mn}(\rho) \mathcal{G}_n^m(\vartheta, \zeta) \quad (28b)$$

$$+ \sum_{n=0}^N \sum_{m=-M}^{-1} Z_{mn}(\rho) \mathcal{G}_n^m(\vartheta, \zeta)$$

$$\lambda(\vartheta, \zeta) = \sum_{n=-N}^{-1} \sum_{m=0}^M \lambda_{mn} \mathcal{G}_n^m(\vartheta, \zeta) \quad (28c)$$

$$+ \sum_{n=0}^N \sum_{m=-M}^{-1} \lambda_{mn} \mathcal{G}_n^m(\vartheta, \zeta)$$

where $\mathcal{G}_n^m(\vartheta, \zeta)$ was defined in (22b). When the radial coordinate is incorporated into the Zernike polynomials, the Fourier-Zernike basis sets for R and Z assuming stellarator symmetry are

$$R(\rho, \vartheta, \zeta) = \sum_{n=-N}^{-1} \sum_{m=-M}^{-1} \sum_{l \in L} R_{lmn} \mathcal{Z}_l^m(\rho, \vartheta) \mathcal{F}^n(\zeta) \quad (29a)$$

$$+ \sum_{n=0}^N \sum_{m=0}^M \sum_{l \in L} R_{lmn} \mathcal{Z}_l^m(\rho, \vartheta) \mathcal{F}^n(\zeta)$$

$$Z(\rho, \vartheta, \zeta) = \sum_{n=-N}^{-1} \sum_{m=0}^M \sum_{l \in L} Z_{lmn} \mathcal{Z}_l^m(\rho, \vartheta) \mathcal{F}^n(\zeta) \quad (29b)$$

$$+ \sum_{n=0}^N \sum_{m=-M}^{-1} \sum_{l \in L} Z_{lmn} \mathcal{Z}_l^m(\rho, \vartheta) \mathcal{F}^n(\zeta).$$

Stellarator symmetry reduces the total number of coefficients exactly in half compared to the general case, so the number of variables required to describe an equilibrium scales as $2M^2N$ (compared to a similar VMEC dimension of $\sim 6M^2N$). Since the force balance equations defined in (12) are functions of R and Z , they also exhibit symmetries when stellarator symmetry is enforced on the inputs:

$$f_\rho(\rho, -\vartheta, -\zeta) = f_\rho(\rho, \vartheta, \zeta) \quad (30a)$$

$$f_\beta(\rho, -\vartheta, -\zeta) = -f_\beta(\rho, \vartheta, \zeta). \quad (30b)$$

E. Nonlinear System Solver

The system of nonlinear equations given by (12) can be written in the form $\mathbf{f} = \mathbf{f}(\mathbf{x})$, where $\mathbf{x} = [R_{lmn}, Z_{lmn}, \lambda_{mn}]^T$ is the state vector that describes the flux surfaces and $\mathbf{f} = [f_\rho^i, f_\beta^i]^T$ contains the force balance errors at a set of collocation points with index i . Since f_ρ and f_β represent the independent components of \mathbf{F} weighted by volume elements, it follows that the L^1 -norm of $\mathbf{f}(\mathbf{x})$ is a numerical approximation to the total force balance error in the plasma volume:

$$\|\mathbf{f}(\mathbf{x})\|_1 \approx \int_0^{2\pi} \int_0^{2\pi} \int_0^1 \|\mathbf{F}(\rho, \vartheta, \zeta)\|_1 \sqrt{g} d\rho d\vartheta d\zeta. \quad (31)$$

Therefore $\mathbf{f}(\mathbf{x}) = \mathbf{0}$ implies that $\mathbf{F}(\rho, \vartheta, \zeta) = \mathbf{0}$, and the corresponding solution \mathbf{x} must represent the equilibrium flux surfaces.

Solving high-dimensional nonlinear systems can be computationally challenging: solutions are not always guaranteed to exist and global convergence often depends strongly on a good initial guess. There is an extensive field of literature on computation methods for these types of problems, but the most popular and robust algorithms are variants of the Newton-Raphson method²⁹. In this iterative procedure, the state vector is updated according to $\mathbf{x}_{k+1} = \mathbf{x}_k + \Delta \mathbf{x}$ where the search direction is defined as

$$\left(\frac{\partial \mathbf{f}}{\partial \mathbf{x}} \bigg|_{\mathbf{x}_k} \right) \Delta \mathbf{x} = -\mathbf{f}(\mathbf{x}_k). \quad (32)$$

The superiority of Newton root-finding algorithms is that they can achieve at least quadratic convergence in the neighborhood of the solution. This is a substantial advantage over other approaches such as the steepest-descent method performed by VMEC to minimize the potential energy of the plasma.

F. Collocation Nodes

The force balance equations $\mathbf{f}(\mathbf{x})$ are solved at discrete points in real space, and there is a lot of flexibility in choosing these interpolation points. The stencil used by the Fast Fourier Transform is equally spaced in $\zeta \in [0, 2\pi)$ and this provides a natural choice for the toroidal grid. An optimal sampling pattern in the polar (ρ, ϑ) domain is unknown for the Zernike basis, but sets have been discovered that minimize the condition number of the resulting Vandermonde matrix^{34,35}. Arranging the nodes into $M+1$ concentric circles with $2m+1$ equally spaced points on each ring m for $m = 0, \dots, M$ helps ensure a uniform distribution of sampling points throughout the domain. The radial locations displayed in Figure 3 are the Chebyshev-Gauss-Lobatto nodes²⁰ (the extrema of Chebyshev polynomials of the first kind) scaled to the domain $\rho \in [0, 1]$ ³⁶. Alternatively, these nodes could have been chosen to avoid rational surfaces or grouped into regions of the plasma volume where more resolution is desired. The radial force balance equation f_ρ is a function of second derivatives in the radial coordinate such as $\partial_{\rho\rho} R$ and

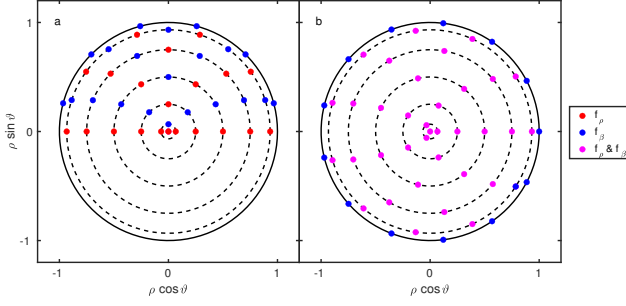


FIG. 3. Interpolation points in the (ρ, ϑ) domain used for the spectral resolution $M = 6$: (a) stellarator symmetry grid (b) non-symmetric grid.

$\partial_{\rho\rho}Z$, which cannot be properly computed at the boundary $\rho = 1$. To avoid numerical issues associated with these values, the grid only evaluates the helical component of the error f_β on the last closed flux surface, which does not require these higher derivatives.

For a general equilibrium calculation, a grid such as the one pictured in Figure 3b would be used at $2N + 1$ toroidal cross-sections equally spaced in the range $\zeta \in [0, 2\pi/N_{FP})$. The use of points with similar (ρ, ϑ) coordinates allows for efficient vectorized computations. If stellarator symmetry is enforced, half of these nodes are redundant and the set of collocation points can be reduced. In the symmetric case only $N + 1$ toroidal angles are used in the range $\zeta \in [0, \pi/N_{FP})$, and the half-grid depicted in Figure 3a is used in the $\zeta = 0$ plane. Note that f_ρ and f_β are sampled on different grids in this cross-section to exploit their unique symmetries. These interpolation nodes are used to calculate the numerical examples in Section IV.

IV. NUMERICAL EXAMPLES

Numerical results of equilibria are presented to validate the described method. Two test cases are shown, which are the same examples also used in the original VMEC paper by Hirshman and Whitson in 1983. The first is an axisymmetric, high-beta, D-shaped plasma, and the second is a high-beta heliotron configuration. Both examples have realistic pressure profiles and rotational transforms that include low-order rational surfaces.

Two error metrics are defined to quantify the accuracy of solutions:

$$\mathcal{E}_X = \langle \|[\Delta R_i, \Delta Z_i]^T\|_2 \rangle \quad (33a)$$

$$\mathcal{E}_F = \int_0^{2\pi} \int_0^{2\pi} \int_0^1 \|F\|_2 \sqrt{g} d\rho d\vartheta d\zeta. \quad (33b)$$

Here ΔR_i and ΔZ_i are the differences in flux surfaces relative to a VMEC equilibrium, and the bracket denotes the mean over the set of points with index i . The VMEC solutions used for comparison were computed with 256 flux surfaces and a residual tolerance of 10^{-16} , with 18 poloidal Fourier modes in

the tokamak case and 12 poloidal and toroidal Fourier modes for the heliotron. Stellarator symmetry was assumed by both VMEC and DESC for all computations. The integral of the force balance error was also numerically approximated using a set of interpolation points. For both error metrics and both test cases, the errors were sampled at thousands of locations throughout the plasma volume and were different from the set of collocation nodes.

The initial guess for the Newton iteration in both cases was obtained by scaling the boundary surface proportional to ρ and setting $\lambda(\vartheta, \zeta) = 0$. Lower resolution solutions were then used as the initial guesses for higher resolution calculations. A Levenberg-Marquardt^{37–39} algorithm was applied, which combines the Newton search direction with the steepest descent direction to improve convergence. The stopping criteria was a minimum step size of $\|\Delta x\|_2 \leq 10^{-4}$.

A. Axisymmetry

The “high-beta, D-shaped plasma” is used as an axisymmetric test case. The fixed boundary and profile inputs are

$$R^b = 3.51 - \cos \theta + 0.106 \cos 2\theta$$

$$Z^b = 1.47 \sin \theta + 0.16 \sin 2\theta$$

$$\iota = 1 - 0.67\rho^2$$

$$p = 1.65 \times 10^3 (1 - \rho^2)^2$$

$$\psi_a = 1$$

which correspond to a tokamak with a volume-averaged beta of approximately 3%. The equilibrium flux surfaces calculated with a resolution of $M = 18$ are plotted and compared to the VMEC solution in Figure 4. The corresponding force balance error is displayed in Figure 5 and normalized to the value of $\|\nabla p(\rho = 0.5)\|_2$. The error is less than 1% throughout the majority of the plasma volume, with most of the error concentrated near the edge where the plasma boundary is prescribed. Figure 6 gives the error metrics, which both display strong convergence rates as M is increased. A toroidal resolution of $N = 0$ is used for all axisymmetric calculations since higher modes are unnecessary.

B. Non-axisymmetry

The “high-beta heliotron” is used as a non-axisymmetric test case, with the fixed boundary and profile inputs:

$$R^b = 10 - \cos \theta - 0.3 \cos(\theta - 19\phi)$$

$$Z^b = \sin \theta - 0.3 \sin(\theta - 19\phi)$$

$$\iota = 1.5\rho^2 + 0.5$$

$$p = 3.4 \times 10^3 (1 - \rho^2)^2$$

$$\psi_a = 1.$$

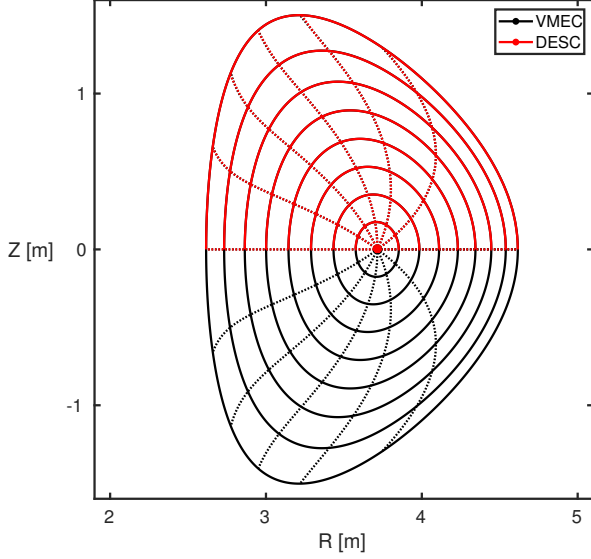


FIG. 4. High-beta, D-shaped tokamak equilibrium. Solid lines show flux surfaces and dotted lines mark curves of constant ϑ . The VMEC equilibrium is displayed in black throughout the full domain, while the the DESC solution with resolution $M = 18$ is plotted in red on $\vartheta \in [0, \pi]$ for comparison.

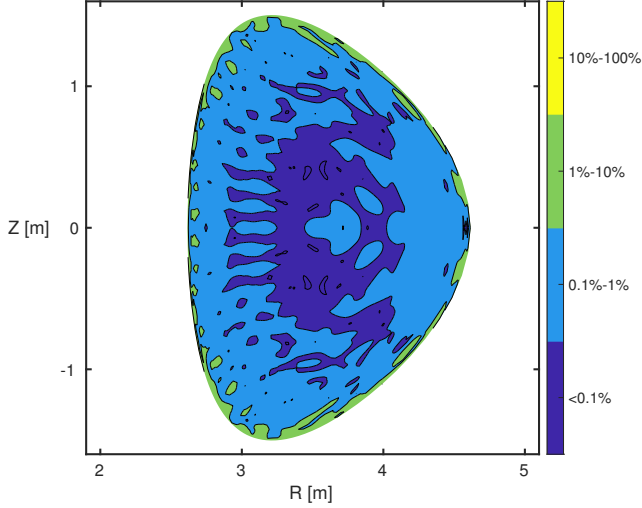


FIG. 5. Normalized force balance error $\|\mathbf{F}\|_2 / \|\nabla p(\rho = 0.5)\|_2$ for the tokamak equilibrium with resolution $M = 18$. Colored regions show the order of magnitude in the percent error.

This is a configuration with a volume-averaged beta of about 2% and a Shafranov shift of about 38 cm relative to the vacuum case. Figure 7 shows a comparison of the equilibrium flux surfaces calculated with a resolution of $M = 18$, $N = 6$ to the VMEC solution. The convergence plot of radial resolution in Figure 8 indicates that this DESC solution with $M = 18$ has a similar magnetic axis location as the VMEC result with 256

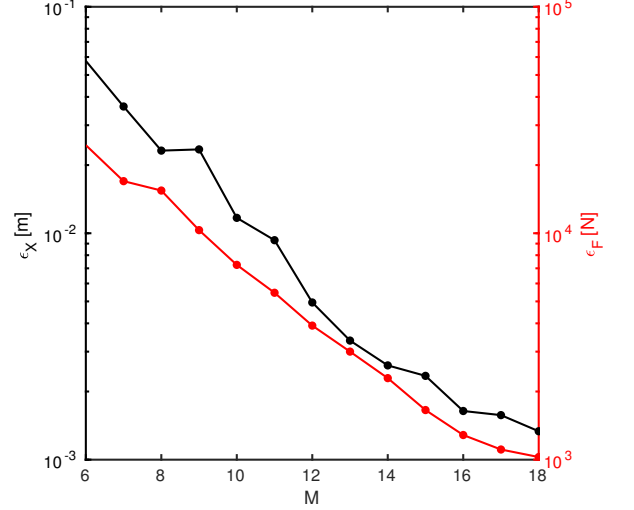


FIG. 6. Convergence plot for the tokamak equilibrium as a function of the Zernike resolutions M . ϵ_X (black) is the average distance between the VMEC and DESC flux surfaces, and ϵ_F (red) is the norm of the force balance error vector integrated over the plasma volume.

flux surfaces. The other convergence plot in Figure 9 shows the two error metrics steadily decreasing as both resolutions increase. The force balance error for the $M = N = 12$ solution is plotted in Figure 10, revealing that the error is below 1% in most of the plasma volume except near the magnetic axis.

C. Discussion

The average discrepancy between the results of DESC and VMEC for the flux surfaces plotted in Figures 4 and 7 is on the order of a few millimeters, as quantified by (33a). The strong trends of ϵ_X in Figures 6 and 9 give confidence that DESC converges to the same equilibrium solution as VMEC. Furthermore, although VMEC is a trusted benchmark, the corresponding convergence of ϵ_F indicates that the results are indeed accurate solutions to the MHD equilibrium equations. The visualization of this accuracy in Figures 5 and 10 are noteworthy because similar self-consistent error calculations are not straightforward in the numerical basis used by VMEC. Furthermore, since VMEC solves the force balance equations indirectly through the energy principle, it may not always converge to a solution with low errors. DESC solves them directly, and the results validate that these equations are being solved properly.

In fixed-boundary calculations, there is a trade-off between solving these equilibrium equations and satisfying the plasma boundary constraints. This tension can explain the concentration of error near the boundary of the “D-shaped plasma,” since many Fourier modes in (ϑ, ζ) coordinates are required to resolve the last closed flux surface of this tokamak. The heliotron has a much simpler elliptical boundary, and the error near the last closed flux surface decreases quickly with only

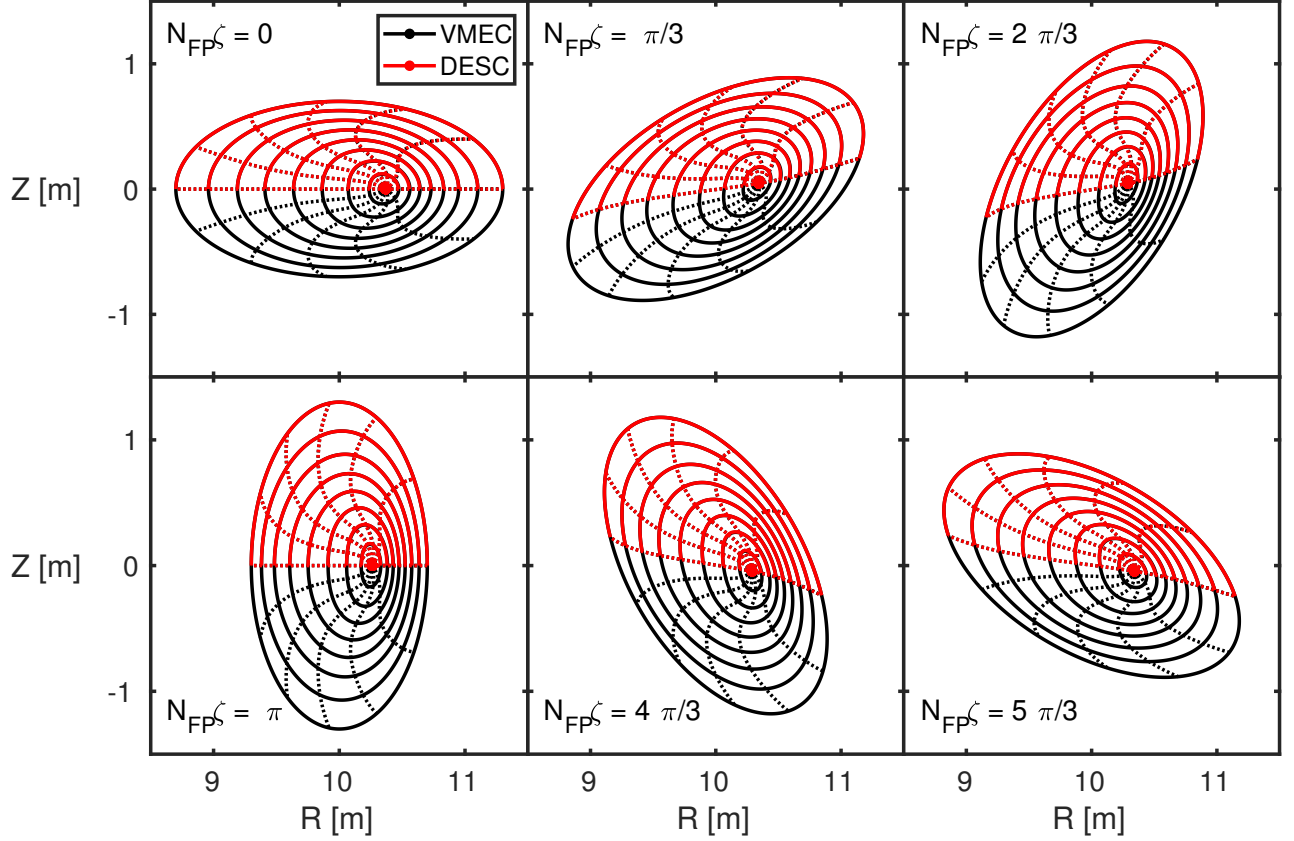


FIG. 7. High-beta heliotron equilibrium. Solid lines show flux surfaces and dotted lines mark curves of constant ϑ . The VMEC equilibrium is displayed in black throughout the full domain, while the the DESC solution with resolution $M = 18$, $N = 6$ is plotted in red on $\vartheta \in [0, \pi]$ for comparison.

a few modes. More modes are required in the core, however, resulting in increased error near the magnetic axis for a given resolution.

DESC is restricted to operating in straight field-line coordinates, which may appear to be a disadvantage compared to the optimal poloidal angle of the VMEC formulation⁴⁰. However, DESC more than compensates for this inefficiency with its compact radial discretization provided by the global basis functions. VMEC's use of radial finite differences uniformly spaced in toroidal magnetic flux results in very poor resolution near the magnetic axis, while the Zernike polynomials inherently satisfy the necessary boundary conditions there. Figure 8 clearly demonstrates that DESC has a superior rate of radial convergence. For the highest resolution shown in which the two codes agree on the magnetic axis location, the dimension of DESC's state vector \mathbf{x} was under 5×10^3 while the total number of variables for VMEC was over 2×10^5 .

In conclusion, DESC is an ideal MHD equilibrium construction code for stellarators. Its approach to solving the equilibrium force balance equations and use of global pseudospectral methods promise to make it more accurate and efficient than existing codes. The code was written in MAT-

LAB to speed up development time, but is now being ported to python to improve computational efficiencies. Future work will include: refined numerical techniques to improve convergence, development of a free-boundary version of the code, and relaxing the assumption on nested flux surfaces to accommodate magnetic islands and stochastic field lines. Future publications will demonstrate the benefits of using DESC in the following applications: resolving rational surfaces, exploring the parameter space of stellarator equilibria, searching for quasi-symmetric solutions, and assessing MHD stability.

SUPPLEMENTARY MATERIAL

The VMEC input files used for the benchmark solutions are included as supplemental materials. The file DSHAPE corresponds to the D-shaped tokamak example, computed with 256 flux surfaces and 18 poloidal Fourier modes. Similarly, the file HELIOTRON corresponds to the heliotron configuration with 256 flux surfaces and 12 poloidal and toroidal Fourier modes.

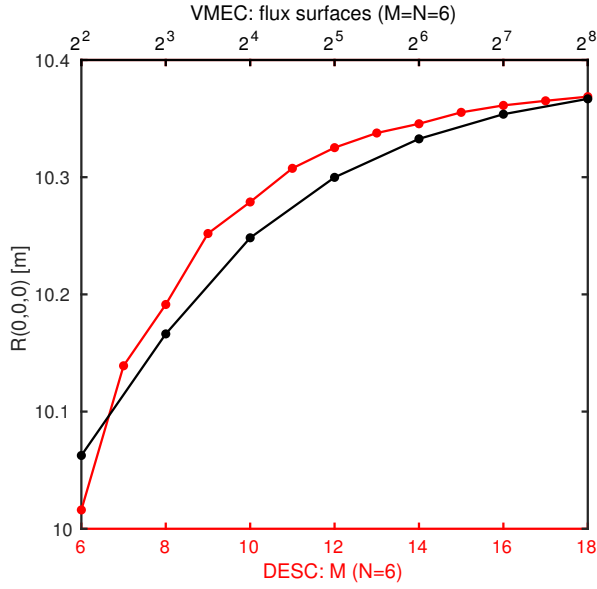


FIG. 8. Convergence of the magnetic axis position in the $\phi = \zeta = 0$ plane for the heliotron equilibrium as a function of radial resolution. The VMEC results (black) are plotted against the number of flux surfaces (top axis), and the DESC results (red) are plotted against the Zernike resolution M (bottom axis).

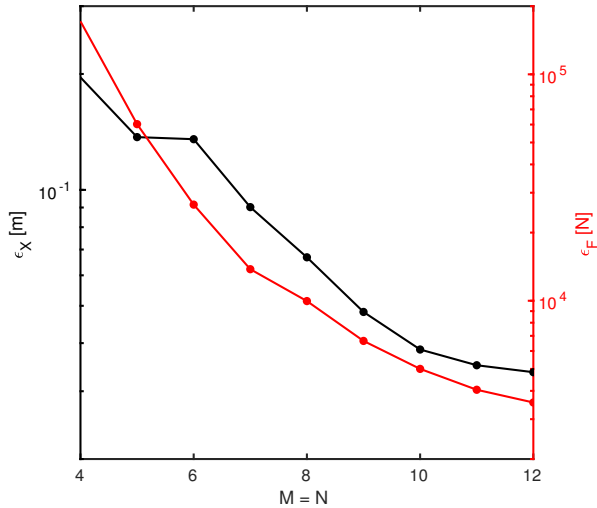


FIG. 9. Convergence plot for the heliotron equilibrium as a function of the spectral resolutions M and N . ϵ_X (black) is the average distance between the VMEC and DESC flux surfaces, and ϵ_F (red) is the norm of the force balance error vector integrated over the plasma volume.

ACKNOWLEDGMENTS

Thank you to Caoxiang Zhu, Sam Lazerson, and Mark Cianciosa for their help with using VMEC and properly interpreting its results. Thank you to Stuart Hudson for insightful

conversations about the challenges of computing ideal MHD stellarator equilibria. This work was supported in part by the United States Department of Energy under contract numbers DE-SC0015878, DE-SC0015480, and DE-SC0020372.

DATA AVAILABILITY

The data that support the findings of this study are available from the corresponding author upon reasonable request. The latest version of the DESC code can be accessed at the public repository: <https://github.com/ddudt/DESC>⁴¹.

Appendix A: Derivation of Force Balance Equations

The following equations outline how to compute the force balance errors f_ρ and f_θ everywhere in the computational domain. Given the Fourier-Zernike coefficients R_{lmn} and Z_{lmn} , the values of $R(\rho, \vartheta, \zeta)$, $Z(\rho, \vartheta, \zeta)$, and all their partial derivatives are known throughout the entire domain from (13a-13b). The covariant basis vectors are defined as

$$\mathbf{e}_\rho = \begin{bmatrix} \partial_\rho R \\ 0 \\ \partial_\rho Z \end{bmatrix} \quad \mathbf{e}_\vartheta = \begin{bmatrix} \partial_\vartheta R \\ 0 \\ \partial_\vartheta Z \end{bmatrix} \quad \mathbf{e}_\zeta = \begin{bmatrix} \partial_\zeta R \\ -R \\ \partial_\zeta Z \end{bmatrix} \quad (\text{A1})$$

and the notation $\mathbf{e}_{\alpha\gamma}$ is used as a shorthand for $\partial_\gamma(\mathbf{e}_\alpha)$. The Jacobian and its partial derivatives are calculated from the basis vectors as

$$\sqrt{g} = \mathbf{e}_\rho \cdot \mathbf{e}_\vartheta \times \mathbf{e}_\zeta \quad (\text{A2a})$$

$$\partial_\rho(\sqrt{g}) = \mathbf{e}_{\rho\rho} \cdot \mathbf{e}_\vartheta \times \mathbf{e}_\zeta + \mathbf{e}_\rho \cdot \mathbf{e}_{\vartheta\rho} \times \mathbf{e}_\zeta + \mathbf{e}_\rho \cdot \mathbf{e}_\vartheta \times \mathbf{e}_{\zeta\rho} \quad (\text{A2b})$$

$$\partial_\vartheta(\sqrt{g}) = \mathbf{e}_{\rho\vartheta} \cdot \mathbf{e}_\vartheta \times \mathbf{e}_\zeta + \mathbf{e}_\rho \cdot \mathbf{e}_{\vartheta\vartheta} \times \mathbf{e}_\zeta + \mathbf{e}_\rho \cdot \mathbf{e}_\vartheta \times \mathbf{e}_{\zeta\vartheta} \quad (\text{A2c})$$

$$\partial_\zeta(\sqrt{g}) = \mathbf{e}_{\rho\zeta} \cdot \mathbf{e}_\vartheta \times \mathbf{e}_\zeta + \mathbf{e}_\rho \cdot \mathbf{e}_{\vartheta\zeta} \times \mathbf{e}_\zeta + \mathbf{e}_\rho \cdot \mathbf{e}_\vartheta \times \mathbf{e}_{\zeta\zeta}. \quad (\text{A2d})$$

The contravariant basis vectors are determined by

$$\mathbf{e}^\rho = \frac{\mathbf{e}_\vartheta \times \mathbf{e}_\zeta}{\sqrt{g}} \quad (\text{A3a})$$

$$\mathbf{e}^\vartheta = \frac{\mathbf{e}_\zeta \times \mathbf{e}_\rho}{\sqrt{g}} \quad (\text{A3b})$$

$$\mathbf{e}^\zeta = \frac{\mathbf{e}_\rho \times \mathbf{e}_\vartheta}{\sqrt{g}}, \quad (\text{A3c})$$

and then the metric coefficients are computed as

$$g^{\rho\rho} = \mathbf{e}^\rho \cdot \mathbf{e}^\rho \quad (\text{A4a})$$

$$g^{\vartheta\vartheta} = \mathbf{e}^\vartheta \cdot \mathbf{e}^\vartheta \quad (\text{A4b})$$

$$g^{\zeta\zeta} = \mathbf{e}^\zeta \cdot \mathbf{e}^\zeta \quad (\text{A4c})$$

$$g^{\vartheta\zeta} = \mathbf{e}^\vartheta \cdot \mathbf{e}^\zeta. \quad (\text{A4d})$$

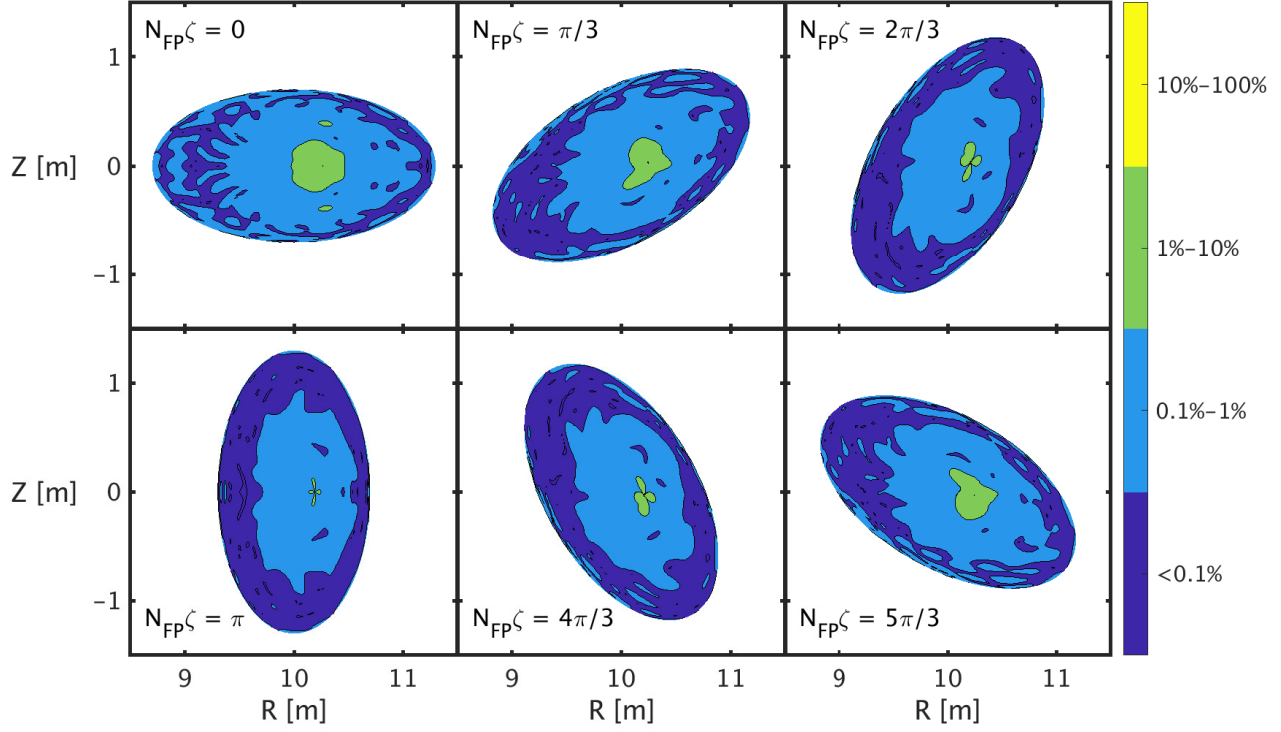


FIG. 10. Normalized force balance error $\|\mathbf{F}\|_2/\|\nabla p(\rho = 0.5)\|_2$ for the high-beta heliotron equilibrium with resolution $M = 12$, $N = 12$. Colored regions show the order of magnitude in the percent error.

Recall that the magnetic field is written in the form

$$\mathbf{B} = B_\rho \mathbf{e}^\rho + B_\vartheta \mathbf{e}^\vartheta + B_\zeta \mathbf{e}^\zeta \quad (\text{A5a})$$

$$= B^\vartheta \mathbf{e}_\vartheta + B^\zeta \mathbf{e}_\zeta, \quad (\text{A5b})$$

and that in the straight field-line coordinates the contravariant components of the field are given by

$$B^\zeta = \frac{\psi'}{2\pi\sqrt{g}} \quad (\text{A6a})$$

$$B^\vartheta = \iota B^\zeta. \quad (\text{A6b})$$

ψ is simply a quadratic function of the flux label by definition: $\psi(\rho) = \psi_a \rho^2$. Therefore, the global magnetic field $\mathbf{B}(\rho, \vartheta, \zeta)$ is entirely known from the coefficients R_{lmn} and Z_{lmn} and the input profile $\iota(\rho)$. The force balance errors can then be calculated directly from this magnetic field. The partial derivatives of the contravariant components are

$$\partial_\rho B^\zeta = \frac{\psi''}{2\pi\sqrt{g}} - \frac{\psi' \partial_\rho(\sqrt{g})}{2\pi g} \quad (\text{A7a})$$

$$\partial_\vartheta B^\zeta = -\frac{\psi' \partial_\vartheta(\sqrt{g})}{2\pi g} \quad (\text{A7b})$$

$$\partial_\zeta B^\zeta = -\frac{\psi' \partial_\zeta(\sqrt{g})}{2\pi g}, \quad (\text{A7c})$$

which are used to compute the partial derivatives of the covariant components:

$$\partial_\rho B_\vartheta = \partial_\rho B^\zeta (\iota \mathbf{e}_\vartheta + \mathbf{e}_\zeta) \cdot \mathbf{e}_\vartheta \quad (\text{A8a})$$

$$+ B^\zeta [(\iota' \mathbf{e}_\vartheta + \iota \mathbf{e}_{\rho\vartheta} + \mathbf{e}_{\zeta\rho}) \cdot \mathbf{e}_\vartheta + (\iota \mathbf{e}_\vartheta + \mathbf{e}_\zeta) \cdot \mathbf{e}_{\vartheta\rho}] \quad (\text{A8b})$$

$$\partial_\rho B_\zeta = \partial_\rho B^\zeta (\iota \mathbf{e}_\vartheta + \mathbf{e}_\zeta) \cdot \mathbf{e}_\zeta \quad (\text{A8b})$$

$$+ B^\zeta [(\iota' \mathbf{e}_\vartheta + \iota \mathbf{e}_{\rho\vartheta} + \mathbf{e}_{\zeta\rho}) \cdot \mathbf{e}_\zeta + (\iota \mathbf{e}_\vartheta + \mathbf{e}_\zeta) \cdot \mathbf{e}_{\zeta\rho}] \quad (\text{A8c})$$

$$\partial_\vartheta B_\rho = \partial_\vartheta B^\zeta (\iota \mathbf{e}_\vartheta + \mathbf{e}_\zeta) \cdot \mathbf{e}_\rho \quad (\text{A8c})$$

$$+ B^\zeta [(\iota \mathbf{e}_{\vartheta\vartheta} + \mathbf{e}_{\zeta\vartheta}) \cdot \mathbf{e}_\rho + (\iota \mathbf{e}_\vartheta + \mathbf{e}_\zeta) \cdot \mathbf{e}_{\rho\vartheta}] \quad (\text{A8d})$$

$$\partial_\vartheta B_\zeta = \partial_\vartheta B^\zeta (\iota \mathbf{e}_\vartheta + \mathbf{e}_\zeta) \cdot \mathbf{e}_\zeta \quad (\text{A8d})$$

$$+ B^\zeta [(\iota \mathbf{e}_{\vartheta\vartheta} + \mathbf{e}_{\zeta\vartheta}) \cdot \mathbf{e}_\zeta + (\iota \mathbf{e}_\vartheta + \mathbf{e}_\zeta) \cdot \mathbf{e}_{\zeta\vartheta}] \quad (\text{A8e})$$

$$\partial_\zeta B_\rho = \partial_\zeta B^\zeta (\iota \mathbf{e}_\vartheta + \mathbf{e}_\zeta) \cdot \mathbf{e}_\rho \quad (\text{A8e})$$

$$+ B^\zeta [(\iota \mathbf{e}_{\vartheta\zeta} + \mathbf{e}_{\zeta\zeta}) \cdot \mathbf{e}_\rho + (\iota \mathbf{e}_\vartheta + \mathbf{e}_\zeta) \cdot \mathbf{e}_{\rho\zeta}] \quad (\text{A8f})$$

$$\partial_\zeta B_\vartheta = \partial_\zeta B^\zeta (\iota \mathbf{e}_\vartheta + \mathbf{e}_\zeta) \cdot \mathbf{e}_\vartheta \quad (\text{A8f})$$

$$+ B^\zeta [(\iota \mathbf{e}_{\vartheta\zeta} + \mathbf{e}_{\zeta\zeta}) \cdot \mathbf{e}_\vartheta + (\iota \mathbf{e}_\vartheta + \mathbf{e}_\zeta) \cdot \mathbf{e}_{\vartheta\zeta}].$$

Ampere's Law then gives the contravariant components of the current density from these partial derivative terms:

$$J^\rho = \frac{\partial_\vartheta B_\zeta - \partial_\zeta B_\vartheta}{\mu_0 \sqrt{g}} \quad (\text{A9a})$$

$$J^\vartheta = \frac{\partial_\zeta B_\rho - \partial_\rho B_\zeta}{\mu_0 \sqrt{g}} \quad (\text{A9b})$$

$$J^\zeta = \frac{\partial_\rho B_\vartheta - \partial_\vartheta B_\rho}{\mu_0 \sqrt{g}}. \quad (\text{A9c})$$

This leads to the evaluation of the two independent components of the force balance vector defined in (11) as $\mathbf{F} = F_\rho \nabla \rho + F_\beta \beta$

$$F_\rho = \sqrt{g} \left(B^\zeta J^\vartheta - B^\vartheta J^\zeta \right) - p' \quad (\text{A10a})$$

$$F_\beta = \sqrt{g} J^\rho \quad (\text{A10b})$$

where the pressure profile $p(\rho)$ is a known input. In order to have both components in the same units and convert the vectors to scalar equations, the magnitudes are used:

$$\|\nabla \rho\|_2 = \|\mathbf{e}^\rho\|_2 = \sqrt{g^{\rho\rho}} \quad (\text{A11a})$$

$$\begin{aligned} \|\beta\|_2 &= \|B^\zeta \mathbf{e}^\vartheta - B^\vartheta \mathbf{e}^\zeta\|_2 \\ &= \sqrt{g^{\vartheta\vartheta} (B^\zeta)^2 + g^{\zeta\zeta} (B^\vartheta)^2 - 2g^{\vartheta\zeta} B^\vartheta B^\zeta}. \end{aligned} \quad (\text{A11b})$$

Directions are also assigned such that $\nabla \rho \cdot \mathbf{e}_\rho > 0$ denotes a positive radial force error and $(\beta \cdot \mathbf{e}_\vartheta) (\beta \cdot \mathbf{e}_\zeta) > 0$ is a positive helical error. These errors are evaluated at discrete points in space and are weighted by the volumes represented by those points, $\sqrt{g} \Delta \rho \Delta \vartheta \Delta \zeta$. This results in the two scalar equations for the force balance error defined in (12):

$$f_\rho = F_\rho \|\nabla \rho\|_2 \sqrt{g} \Delta \rho \Delta \vartheta \Delta \zeta \text{sign}(\nabla \rho \cdot \mathbf{e}_\rho) \quad (\text{A12a})$$

$$f_\beta = F_\beta \|\beta\|_2 \sqrt{g} \Delta \rho \Delta \vartheta \Delta \zeta \text{sign}(\beta \cdot \mathbf{e}_\vartheta) \text{sign}(\beta \cdot \mathbf{e}_\zeta). \quad (\text{A12b})$$

Special attention must be given to the magnetic axis since the Jacobian \sqrt{g} vanishes at the coordinate origin. The contravariant components of the magnetic field are physical quantities that have finite values at the magnetic axis but have an indeterminate form at $\rho = 0$. These components and their derivatives are resolved by applying l'Hospital's rule, multiple times in some cases:

$$B^\zeta(\rho = 0) = \frac{\psi''}{2\pi \partial_\rho(\sqrt{g})} \quad (\text{A13a})$$

$$B^\vartheta(\rho = 0) = \frac{\iota \psi''}{2\pi \partial_\rho(\sqrt{g})} \quad (\text{A13b})$$

$$\partial_\rho B^\zeta(\rho = 0) = -\frac{\psi'' \partial_{\rho\rho}(\sqrt{g})}{4\pi (\partial_\rho(\sqrt{g}))^2} \quad (\text{A13c})$$

$$\partial_\vartheta B^\zeta(\rho = 0) = 0 \quad (\text{A13d})$$

$$\partial_\zeta B^\zeta(\rho = 0) = -\frac{\psi'' \partial_{\zeta\rho}(\sqrt{g})}{2\pi (\partial_\rho(\sqrt{g}))^2}. \quad (\text{A13e})$$

Together with the contravariant basis vector equation

$$\mathbf{e}^\rho(\rho = 0) = \frac{\mathbf{e}_{\vartheta\rho} \times \mathbf{e}_\zeta}{\partial_\rho(\sqrt{g})} \quad (\text{A14})$$

the radial force balance error equation (A12a) can be computed at the magnetic axis. The helical error (A12b) needs further treatment because

$$\lim_{\rho \rightarrow 0} F_\beta = 0 \quad (\text{A15a})$$

$$\lim_{\rho \rightarrow 0} \|\beta\|_2 = \infty. \quad (\text{A15b})$$

Applying l'Hospital's rule to this combined term yields

$$(F_\beta \|\beta\|_2) \Big|_{\rho=0} = \frac{\partial_{\vartheta\rho} B_\zeta - \partial_{\zeta\rho} B_\vartheta}{\mu_0 \partial_\rho(\sqrt{g})} \sqrt{(\mathbf{e}_\zeta \times \mathbf{e}_\rho) \cdot (\mathbf{e}_\zeta \times \mathbf{e}_\rho) (B^\zeta)^2}, \quad (\text{A16})$$

where the mixed partial derivatives of the covariant field components are defined at the magnetic axis by

$$\partial_{\vartheta\rho} B_\zeta(\rho = 0) = \partial_{\vartheta\rho} B^\zeta \mathbf{e}_\zeta \cdot \mathbf{e}_\zeta + B^\zeta (\iota \mathbf{e}_{\vartheta\rho} + 2\mathbf{e}_{\zeta\rho}) \cdot \mathbf{e}_\zeta \quad (\text{A17a})$$

$$\partial_{\zeta\rho} B_\vartheta(\rho = 0) = \partial_{\zeta\rho} B^\zeta \mathbf{e}_\zeta \cdot \mathbf{e}_{\vartheta\rho} + B^\zeta (\mathbf{e}_{\zeta\zeta} \cdot \mathbf{e}_{\vartheta\rho} + \mathbf{e}_\zeta \cdot \mathbf{e}_{\vartheta\zeta\rho}) \quad (\text{A17b})$$

and the mixed contravariant derivative becomes

$$\partial_{\vartheta\rho} B^\zeta = \frac{\psi'' (2\partial_{\rho\rho}(\sqrt{g}) \partial_{\vartheta\rho}(\sqrt{g}) - \partial_\rho(\sqrt{g}) \partial_{\vartheta\rho\rho}(\sqrt{g}))}{4\pi (\partial_\rho(\sqrt{g}))^3}. \quad (\text{A18})$$

Equations (A13c), (A13e), and (A18) depend on higher-order derivatives of \sqrt{g} , and the only nonzero terms in these expressions at the magnetic axis are

$$\begin{aligned} \partial_{\rho\rho}(\sqrt{g}) &= 2\partial_\rho R (\partial_{\rho\vartheta} Z \partial_\rho R - \partial_{\rho\vartheta} R \partial_\rho Z) \\ &\quad + R (\partial_\rho R \partial_{\rho\rho\vartheta} Z - \partial_\rho Z \partial_{\rho\rho\vartheta} R) \\ &\quad + R (2\partial_{\rho\rho} R \partial_{\rho\vartheta} Z - 2\partial_{\rho\vartheta} R \partial_{\rho\rho} Z) \end{aligned} \quad (\text{A19a})$$

$$\begin{aligned} \partial_{\zeta\rho}(\sqrt{g}) &= \partial_\zeta R (\partial_\rho R \partial_{\rho\vartheta} Z - \partial_{\rho\vartheta} R \partial_\rho Z) \\ &\quad + R (\partial_{\zeta\rho} R \partial_{\rho\vartheta} Z + \partial_\rho R \partial_{\zeta\rho\vartheta} Z) \\ &\quad - R (\partial_{\zeta\rho\vartheta} R \partial_\rho Z + \partial_{\rho\vartheta} R \partial_{\zeta\rho} Z) \end{aligned} \quad (\text{A19b})$$

$$\begin{aligned} \partial_{\zeta\rho}(\sqrt{g}) &= \partial_\zeta R (\partial_{\rho\vartheta} Z \partial_\rho R - \partial_{\rho\vartheta} R \partial_\rho Z) \\ &\quad + R (\partial_{\zeta\rho} R \partial_{\rho\vartheta} Z + \partial_\rho R \partial_{\zeta\rho\vartheta} Z) \\ &\quad - R (\partial_{\zeta\rho\vartheta} R \partial_\rho Z + \partial_{\rho\vartheta} R \partial_{\zeta\rho\vartheta} Z) \end{aligned} \quad (\text{A19c})$$

$$\begin{aligned} \partial_{\vartheta\rho\rho}(\sqrt{g}) &= 2\partial_{\rho\vartheta} R (\partial_{\rho\vartheta} Z \partial_\rho R - \partial_{\rho\vartheta} R \partial_\rho Z) \\ &\quad + 2\partial_\rho R (\partial_{\rho\vartheta\vartheta} Z \partial_\rho R - \partial_{\rho\vartheta\vartheta} R \partial_\rho Z) \\ &\quad + R (\partial_\rho R \partial_{\rho\rho\vartheta\vartheta} Z - \partial_\rho Z \partial_{\rho\rho\vartheta\vartheta} R) \\ &\quad + 2R (\partial_{\rho\rho} R \partial_{\rho\vartheta\vartheta} Z - \partial_{\rho\rho} Z \partial_{\rho\vartheta\vartheta} R) \\ &\quad - R (\partial_{\rho\vartheta} R \partial_{\rho\rho\vartheta} Z - \partial_{\rho\vartheta} Z \partial_{\rho\rho\vartheta} R). \end{aligned} \quad (\text{A19d})$$

Finally, a nonzero value must be used for the Jacobian when calculating the volume of the torus surrounding the magnetic axis denoted by $\sqrt{g} \Delta \rho \Delta \vartheta \Delta \zeta$.

Appendix B: List of Variables

Table I lists a summary of all the variables and their units.

TABLE I. List of variables.

Symbol	Variable	Units
R, ϕ, Z	toroidal coordinates	m, rad, m
ρ, ϑ, ζ	straight field-line coordinates	none, rad, rad
$\mathbf{e}_\rho, \mathbf{e}_\vartheta, \mathbf{e}_\zeta$	covariant basis vectors	m
$\mathbf{e}^\rho, \mathbf{e}^\vartheta, \mathbf{e}^\zeta$	contravariant basis vectors	m ⁻¹
\sqrt{g}	flux coordinates Jacobian	m ³
$\lambda(\vartheta, \zeta)$	straight field-line stream function	rad
$\psi(\rho), \chi(\rho)$	toroidal and poloidal magnetic flux	Wb
$\mathbf{r}(\rho)$	rotational transform	none
$p(\rho)$	pressure	Pa
μ_0	magnetic constant	H m ⁻¹
\mathbf{B}	magnetic field	T
\mathbf{J}	current density	A m ⁻²
\mathbf{F}	force balance error vector	N m ⁻³
f_ρ, f_β	force balance error equations	N
\mathbf{x}	state vector of independent variables	m, rad
\mathbf{f}	system of equations to minimize	N
M	maximum poloidal Fourier mode	none
N	maximum toroidal Fourier mode	none
N_{FP}	number of toroidal field periods	none

- ¹L. L. Lao, H. St. John, and R. D. Stambaugh, Nucl. Fusion **25**, 1611–1622 (1985).
²L. Spitzer, Phys. Fluids **1**, 253–264 (1958).
³A. Dinklage, C. D. Beidler, P. Helander, G. Fuchert, H. Maaßberg, K. Rahbarnia, T. Sunn Pedersen, Y. Turkin, R. C. Wolf, A. Alonso, *et al.*, Nature Phys. **14**, 855–860 (2018).
⁴M. D. Kruskal and R. M. Kulsrud, Phys. Fluids **1**, 265–274 (1958).
⁵R. Chodura and A. Schlüter, J. Comput. Phys. **41**, 68–88 (1981).
⁶F. Bauer, O. Betancourt, and P. Garabedian, *A Computational Method in Plasma Physics*, edited by W. Beiglbock, H. Canannes, and S. A. Orszag, Springer Series in Computational Physics (Springer-Verlag, 1978).
⁷U. Schwenn, Comput. Phys. Commun. **31**, 167–199 (1984).
⁸A. Bhattacharjee, J. C. Wiley, and R. L. Dewar, Comput. Phys. Commun. **31**, 213–225 (1984).
⁹T. C. Hender, B. A. Carreras, L. Garcia, and J. A. Rome, J. Comput. Phys. **60**, 76–96 (1985).
¹⁰S. P. Hirshman and J. C. Whitson, Phys. Fluids **26**, 3553–3568 (1983).

- ¹¹S. A. Lazerson, J. Loizu, S. Hirshman, and S. R. Hudson, Phys. Plasmas **23** (2016).
¹²O. Betancourt, Comm. Pure Appl. Math. **41**, 551–568 (1988).
¹³K. Harafuji, T. Hayashi, and T. Sato, J. Comput. Phys. **81**, 169–192 (1989).
¹⁴A. Reiman and H. Greenside, Comput. Phys. Commun. **43**, 157–167 (1986).
¹⁵S. P. Hirshman, R. Sanchez, and C. R. Cook, Phys. Plasmas **18** (2011).
¹⁶S. R. Hudson, R. L. Dewar, G. Dennis, M. J. Hole, M. McGann, G. von Nessi, and S. Lazerson, Phys. Plasmas **19** (2012).
¹⁷R. C. Grimm, J. M. Greene, and J. L. Johnson, “Computation of the magnetohydrodynamic spectrum in axisymmetric toroidal confinement systems,” in *Methods in Computational Physics: Advances in Research and Applications*, Vol. 16, edited by S. Fernbach, M. Rotenberg, and J. Killeen (Academic Press, Inc, New York, 1976) pp. 253–280.
¹⁸W. D. D’haeseleer, W. N. G. Hitchon, J. D. Callen, and J. L. Shohet, *Flux Coordinates and Magnetic Field Structure*, edited by R. Glowinski, M. Holt, P. Hut, H. B. Keller, J. Killeen, S. A. Orszag, and V. V. Rusanov, Springer Series in Computational Physics (Springer-Verlag, 1991).
¹⁹A. H. Boozer, Rev. Mod. Phys. **76**, 1075–1079 (2005).
²⁰J. P. Boyd, *Chebyshev and Fourier Spectral Methods* (Dover Publications, Inc, New York, 2000).
²¹F. Zernike, Mon. Not. R. Astron. Soc. **94**, 377–384 (1934).
²²T. Sakai and L. G. Redekopp, J. Comput. Phys. **228**, 7069–7085 (2009).
²³T. Matsushima and P. S. Marcus, J. Comput. Phys. **120**, 365–374 (1995).
²⁴W. T. M. Verkleij, J. Comput. Phys. **136**, 100–114 (1997).
²⁵V. Lakshminarayanan and A. Fleck, J. Modern Optics **58**, 545–561 (2011).
²⁶J. Loomis, ASTM STP **666**, 71–86 (1978).
²⁷V. L. Genberg, G. J. Michels, and K. B. Doyle, Proc SPIE **4771**, 276–286 (2002).
²⁸J. P. Boyd and F. Yu, J. Comput. Phys. **230**, 1408–1438 (2011).
²⁹W. H. Press, B. P. Flannery, S. A. Teukolsky, and W. T. Vetterling, *Numerical Recipes: The Art of Scientific Computing* (Cambridge University Press, 1989).
³⁰H. R. Lewis and P. M. Bellan, J. Math. Phys. **31**, 2592–2596 (1990).
³¹S. A. Orszag, J. Atmos. Sci. **28**, 1074 (1971).
³²D. K. Lee, J. H. Harris, S. P. Hirshman, and G. H. Neilson, Nucl. Fusion **28**, 1351–1364 (1988).
³³R. L. Dewar and S. R. Hudson, Physica D **112**, 275–280 (1998).
³⁴J. M. Carnicer and C. Godes, Numer. Algor. **66**, 1–16 (2014).
³⁵D. Ramos-Lopez, M. A. Sanchez-Granero, M. Fernandez-Martinez, and A. Martinez-Finkelshtein, Appl. Math. Comput. **274**, 247–257 (2016).
³⁶L. N. Trefethen, *Finite Difference and Spectral Methods for Ordinary and Partial Differential Equations* (Cornell University, 1996).
³⁷K. Levenberg, Q. Appl. Math. **2**, 164–168 (1944).
³⁸D. Marquardt, SIAM J. Appl. Math. **11**, 431–441 (1963).
³⁹J. J. Moré, “The levenberg-marquardt algorithm: Implementation and theory,” in *Numerical Analysis*, edited by G. A. Watson (Springer, 1978) pp. 105–116.
⁴⁰S. P. Hirshman and J. Breslau, Phys. Plasmas **5**, 2664–2675 (1998).
⁴¹D. W. Dudt and E. Kolemen, “DESC,” <https://github.com/ddudt/DESC> (2020).